analytical chemistry

pubs.acs.org/ac Article

Transparent Ultramicroelectrodes for Studying Interfacial Charge-Transfer Kinetics of Photoelectrochemical Water Oxidation at TiO_2 Nanorods with Scanning Electrochemical Microscopy

Xiao Li and Shanlin Pan*

Cite This: *Anal. Chem.* 2021, 93, 15886−15896 Read Online

ACCESS | Metrics & More | Article Recommendations | Supporting Information

ABSTRACT: Scanning electrochemical microscopy (SECM) has been extensively applied to the electrochemical analysis of the surfaces and interfaces of a photoelectrochemical (PEC) system. A semiconductor photoelectrode with a well-defined geometry and active surface area comparable to SECM's tip is highly desired for accurately quantifying interfacial charge-transfer activities and photoelectrochemically generated redox species, where the broadening effects due to the mass transfer gradient and nonlocal electron transfer at a planar semiconductor surface can be minimized. Here, we present a newly developed platform as a SECM substrate for investigating semiconductor PEC activities, which is based on a transparent ultramicroelectrode (UME) fabricated by using two-step photolithographic patterning and ion milling methods. This transparent UME with a 25 μm recessed disk shape is fully characterized with SECM for quantifying the interfacial charge-transfer rates of $IrCl_6^{2-}/IrCl_6^{3-}$ by comparing with theoretical results from finite element simulations in COMSOL Multiphysics. When coated with TiO_2 nanorods as a model semiconductor material, the transparent UME can be used to quantify the catalytic PEC water oxidation in a feedback mode of SECM by sampling tip and substrate current signals simultaneously. This transparent UME−SECM study provides insights into the potential-dependent PEC water oxidation reaction mechanism and the quantitative analysis of photocurrent contributions from water oxidation and the SECM tip-generated redox mediator. The transparent UME−SECM method can be potentially expanded to other SECM operation modes such as surface interrogation for understanding the dynamics of the electrode surfaces and interfaces of a PEC system.

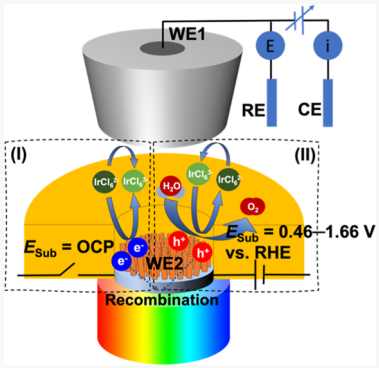

INTRODUCTION

Photoelectrochemical (PEC) technologies have been developed for quantitative analysis such as molecular sensing,[1−3] cell imaging,[4] and solar energy harvesting and conversion.[5−7] TiO_2 is one of the most extensively studied semiconductors for PEC-enabled water splitting,[8] biosensing,[9,10] and photosynthesis[11,12] due to its earth abundance, nontoxicity, high chemical stability, and photocorrosion resistance.[13,14] The detection sensitivity and energy conversion efficiency of a PEC system mainly depend on the efficiencies of light absorption, charge carrier generation, separation and transport at the electrode/electrolyte interface, and redox reaction kinetics at the surface of a PEC electrode. This leads to the need to develop advanced surface and interfacial electroanalytical techniques for quantitatively resolving these PEC activities.

Scanning electrochemical microscopy (SECM) developed by Bard's group has been reported to be a powerful tool for interfacial electrochemical analysis in PEC systems.[15] The operation principle of the SECM technique is based on a scanning ultramicroelectrode (UME) tip probing the local electrochemical interactions with a substrate electrode surface. It operates in a variety of modes such as feedback,[16] generation-collection,[17] surface interrogation,[18] hopping,[19] redox competition,[20] tunneling,[21] and so forth to obtain mass transfer and surface reaction kinetic information of an electrode surface. The use of an UME tip with a size of 25 μm or less enables the quantitative electroanalysis with improved temporal[22,23] and spatial resolutions.[24−27] For instance, SECM was used to study the PEC activities of TiO_2 in the presence of redox mediators of $Fe(CN)_6^{4-}/Fe(CN)_6^{3-}$.[28] The surface chemistry activities of photogenerated charge carriers at an unbiased TiO_2 substrate were revealed by illustrating the tip-to-substrate distance dependence of the tip current feedback. SECM has also been applied to investigate charge-transfer kinetics and product detection at visible light-sensitive photoelectrodes such as CdS,[29] Eosin Y-sensitized ZnO,[30] Mo−$BiVO_4$,[31,32] CdS-sensitized ZnO,[33] rGO/Bi_2WO_6/Au,[34] g-C_3N_4/ZnTe heterojunctions,[35] and Co−B_i-modified $BiVO_4$.[36] The tip current responses in these studies are

Received: June 21, 2021
Accepted: November 10, 2021
Published: November 24, 2021

https://doi.org/10.1021/acs.analchem.1c02598
Anal. Chem. 2021, 93, 15886−15896

sensitive to the tip-to-substrate distance, substrate potential, some other characteristics of the substrate (e.g., light absorptivity, surface chemistry kinetics, and charge carrier density and its recombination and separation), and side reactions from water splitting and its products. The entire planar substrate is illuminated with a light source in these studies, while only a small region is probed by an UME. This SECM configuration would not provide an accurate quantification of surface charge-transfer activities at a semiconductor due to the mass-transfer concentration gradient of redox species at the planar electrode surface, nonlocal electron transfer at extended active surfaces, and significant substrate edge effects.[37,38] Although these issues are less likely to be concerned for a semiconductor substrate in the dark because of the low density of thermally excited charge carrier density, they become prominent for a photoexcited semiconductor under PEC reaction conditions.

The issues of heterogeneous electron transfer at a conventional planar electrode system can be partially addressed by utilizing a miniaturized light source to produce a confined photoexcited region on the surface of the planar electrode. For example, an optical fiber can be used to study the local photocatalytic performance of the photocatalyst substrate.[39−46] Our group recently reported a fast screening of PEC water oxidation activity at Co−$BiVO_4$ and Au-modified hematite photocatalyst spots (∼200 μm in diameter) with an optical fiber-equipped SECM.[45,46] Conzuelo et al.[47] and Bae et al.[48] developed dual electrochemical/optical UME tips, which substantially reduced the background photocatalytic signals achieving a high lateral resolution. A focused micrometer-sized laser beam was incorporated by Willets and Rodriguez-Lopez as light source under the tip of SECM for probing the localized interfacial plasmon-mediated reactions.[49−51] A restricted illumination area can also be used for local PEC studies as shown by a recent SECM study of the hematite substrate through a ∼10 μm pinhole.[52] This method however could not provide individually addressable photocatalytic responses due to the possible electron transfer at the biased nonlocal surfaces.

Recent studies suggest that the semiconductor photoelectrode with a confined surface area can fully address the above issues. Bard and co-workers have reported the applications of >200 μm photoelectrodes of TiO_2[53] and W/Mo−$BiVO_4$[54] sealed with a thin insulating film in the SECM-based PEC studies, where the individually addressable photoelectrodes with the electrically isolated active area proved to be an ideal electrode configuration to prevent heterogeneous electron-transfer activities. This electrode configuration can be easily achieved through the conventional microfabrication technology for Si UMEs[55] and our recent work of transparent indium tin oxide (ITO) UMEs (10 μm in diameter).[56,57]

Here, we successfully fabricated planar ITO and fluorine-doped tin oxide (FTO) UMEs (25 μm in diameter) with a methodology of a two-step photolithographic patterning incorporated with an ion milling treatment. This transparent and well-defined UME platform was for the first time used as a substrate in SECM to quantitatively investigate the heterogeneous charge-transfer kinetics at the electrode/electrolyte interface. A model semiconductor-based PEC system is built on the in situ grown TiO_2 UME on FTO for the electrochemical analysis of potential-dependent interfacial kinetics in PEC water oxidation. This transparent UME platform can be potentially expanded to characterize other PEC systems and used for accurate analysis of local redox reaction mechanism and and molecular sensing.

MATERIALS AND METHODS

Reagents and Materials. All chemicals and solvents were used as received without any further purification. Titanium(IV) butoxide (>99%) and potassium hexachloroiridate(IV) (Ir > 39%) were purchased from Alfa Aesar. Hydrochloric acid (37% wt), sodium sulfate anhydrous, isopropanol (≥99.5%), acetone (≥99.5%), and ethanol (≥95%) were purchased from VWR. ITO-coated glass (<15 Ω/sq.) was bought from Colorado Concept Coatings, LLC. FTO-coated glass (TEC15, <15 Ω/sq.) was obtained from Pilkington. A customized photomask for photolithographic fabrication was supplied by Photo Sciences Inc.

ITO/FTO UME Fabrication. Figure 1 illustrates the fabrication procedures of ITO/FTO UMEs mainly involving

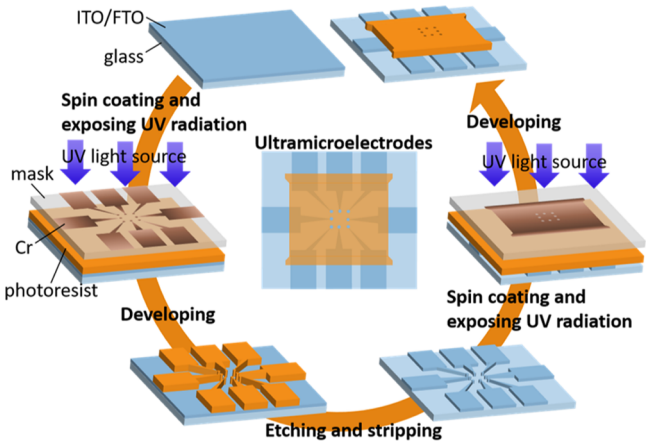

Figure 1. Schematic of the fabrication of transparent ITO/FTO UMEs via photolithography and ion milling.

two photolithographic steps and an ion milling treatment in between, which is similar to the method employed in our recent publication.[56] First, a 20 mm × 20 mm squared ITO- or FTO-coated glass slide was cleaned by sequential sonication in a detergent solution, acetone, ethanol, and deionized (DI) water, respectively, and a following UV-O_3 treatment (UV/ozone procleaner, Bioforce Nanosciences). In the first photolithographic step, a layer of a Shipley S1818 photoresist was coated on an ITO/FTO glass slide with a Solitec spin coater. An MA-6 mask aligner (Karl Suss) was used to transfer the pattern from a customized photomask to the photoresist layer by emitting UV radiation. After developing in the Shipley MF-319 developer, a photoresist layer of eight center-patterned holes connected with eight exterior rectangular blocks was created and used to protect the underlying conductive surfaces during the following ion milling. Then, the sample was treated using an ion-milling system (Intelvac and Four-Wave) to remove the ITO/FTO layer at the exposed surfaces. The remaining photoresist was stripped off by sonicating in acetone and isopropanol, respectively. Finally, a second photolithographic step was utilized to expose eight centralized micrometer holes and the exterior portion for electrical connection, followed by development and hard baking to form eight isolated transparent ITO/FTO UMEs sealed by the photoresist. These UMEs were annealed under an optimized hard baking condition of 300 °C for 30 min

https://doi.org/10.1021/acs.analchem.1c02598
Anal. Chem. 2021, 93, 15886−15896

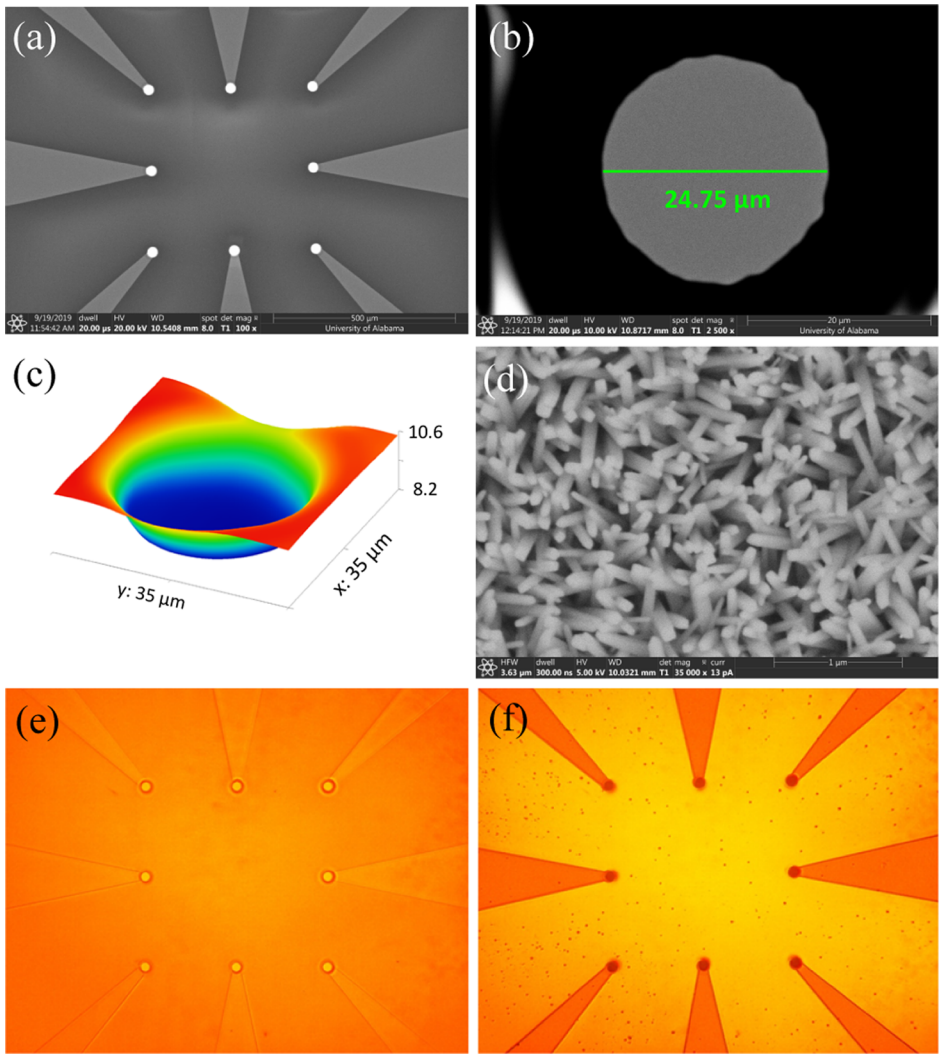

Figure 2. SEM images of (a) ITO UMEs and (b) single ITO UME. (c) 3D AFM image of an ITO UME. (d) SEM image of TiO_2 nanorods in situ grown on FTO. Optical microscopy images of (e) FTO UMEs and (f) TiO_2–FTO UMEs.

under a N_2 atmosphere to achieve the highest resistance to the electrolyte and surface scratching.

TiO_2–FTO UME Fabrication. After the etching and stripping steps, a typical hydrothermal process and annealing were used to in situ grow TiO_2 on a patterned FTO substrate. Specifically, the sample was sited vertically at the bottom of a 25 mL stainless-steel Teflon-lined autoclave. The hydrothermal solution containing 0.3 mL of titanium(IV) butoxide in 20 mL of 18.5% wt. HCl was transferred to the autoclave and heated in an electric oven at 180 °C for 4 h. After being cooled down to room temperature, samples were completely rinsed with DI water and then annealed at 600 °C in air for 2 h. A second photolithographic step was performed with the same procedures as described above to obtain recessed disk-shaped TiO_2-coated FTO UMEs. TiO_2 in situ grown on ITO can also be prepared by the hydrothermal process and annealing under appropriate conditions.[58]

Electrode Characterization. The size and geometry of the as-fabricated UMEs were characterized by using scanning electron microscopy (SEM, Apreo, Thermo Fisher Scientific), atomic force microscopy (AFM) (Mad City Labs) equipped with an Akiyama probe (NANOSENSORS), and an AmScope microscope digital camera (1.3 MP, MU 130, AmScope).

Electrochemical and PEC SECM Setup. The electrochemical and PEC measurements were performed based on a CHI 920c bipotentiostat/SECM system (CH Instruments) equipped with a halogen lamp (TH4-100, Olympus, 98.27 mW/cm^2) and an electron-multiplying charge-coupled device (EMCCD) camera (iXon X3 DU-897E, Andor Technology). A 10 μm (in diameter) disk-shaped Pt UME (RG ~3.5) was employed as the SECM tip electrode. A platinum wire and a Ag wire or Ag/AgCl (Sat'd KCl) were used as the counter electrode (CE) and reference electrode, respectively. The electrolyte solutions employed include 0.1 M Na_2SO_4 containing 1 mM K_2IrCl_6 (pH 4.5) and redox-free 0.1 M Na_2SO_4 (pH 5.8). All the electrode potential values presented in this work are corrected to be versus the reversible hydrogen electrode (RHE). The light intensity focused on samples was measured with a digital power meter (Newport Power Meter 1931-C). More details of the adopted SECM system can be found in Figures S1 and S2.

COMSOL Multiphysics Simulation. Finite element simulations[59,60] of voltammetric behaviors, local concentration profiles of redox molecules at an UME, and current–potential–distance relationships (i.e., approach curves) were performed with COMSOL Multiphysics software (Version

https://doi.org/10.1021/acs.analchem.1c02598
Anal. Chem. 2021, 93, 15886–15896

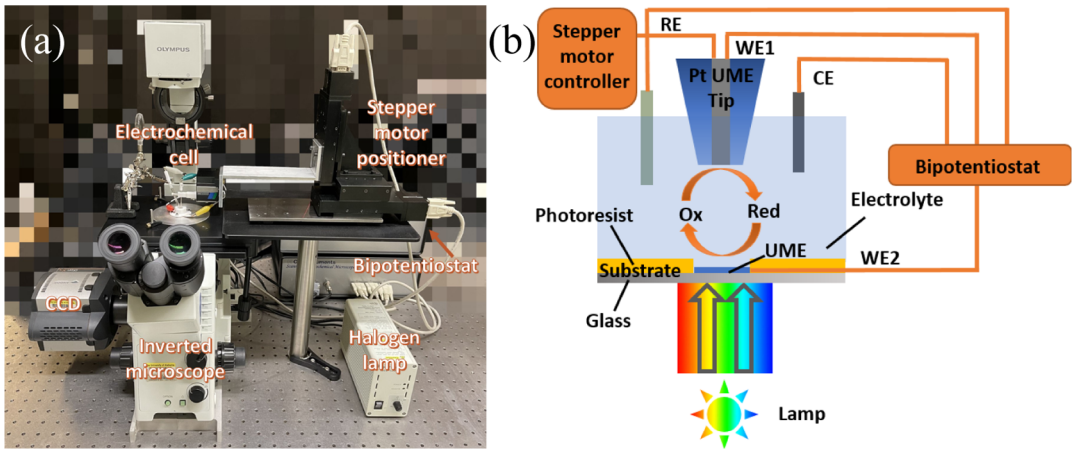

Figure 3. Digital photo (a,b) schematic of the SECM setup for investigating surface electrochemical activities under PEC conditions with a microfabricated UME substrate.

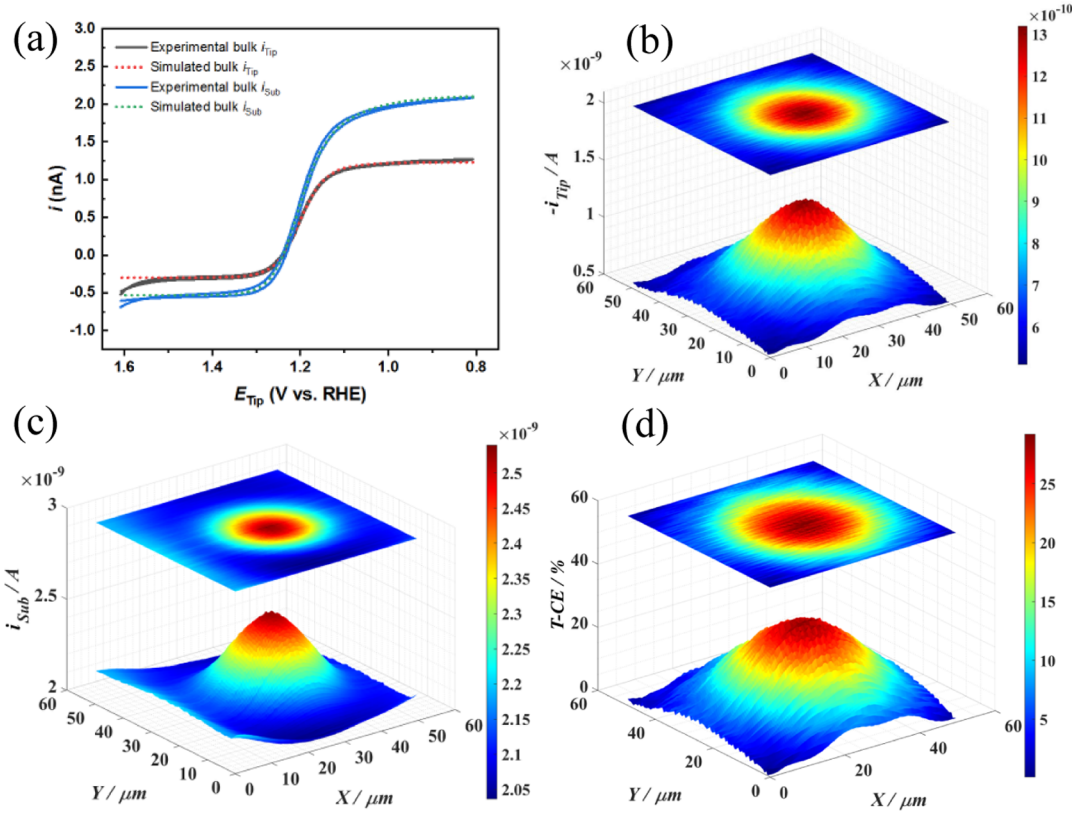

Figure 4. (a) Bulk CV curves of the Pt tip and the ITO UME substrate in 0.1 M Na_2SO_4 containing 1 mM K_2IrCl_6 and simulated data by fitting with the COMSOL Multiphysics finite element method. Scan rate: 10 mV s^{-1}. SECM reactivity images (50 × 50 μm) of (b) i_{Tip} and (c) i_{Sub} under the constant-height substrate generation tip collection (SG-TC) mode at d = 15 μm over the ITO UME. E_{Sub} = 0.91 V (vs RHE) and E_{Tip} = 1.51 V (vs RHE). Scan rate: 25 μm s^{-1}. (d) Mapping of tip T-CE extracted from (b,c) over the ITO UME. Top images in (b−d) represent the projections onto the *xy*-plane.

5.4). Principles of modeling and simulation are further introduced in Figure S3.

RESULTS AND DISCUSSION

Fabrication of Bare and TiO_2 Nanorods-Modified UMEs. As shown in the SEM image (Figure 2a), eight disk-shaped conductive ITO UMEs are formed on a single ITO glass slide with their electrical contacts buried under the photoresist layer. The triangular-shaped areas are the underlying electrical connection to each ITO UME. Digital photos of real samples give a better view of the transparent substrate and the yellow ochre photoresist layer (Figure S4). At a higher magnification of SEM, the individual ITO UME shows a smooth and clean surface with a diameter of 24.75 μm (r_{Sub} = 12.375 μm, Figure 2b). AFM further revealed a recessed disk shape of the ITO UME (Figure 2c). A 2.38 μm thickness of the photoresist layer (t_{pr}) was obtained by the AFM depth profile analysis (Figure S5). Our methodology enables the fabrication of an array of electrically isolated UMEs at a time to

https://doi.org/10.1021/acs.analchem.1c02598
Anal. Chem. 2021, 93, 15886−15896

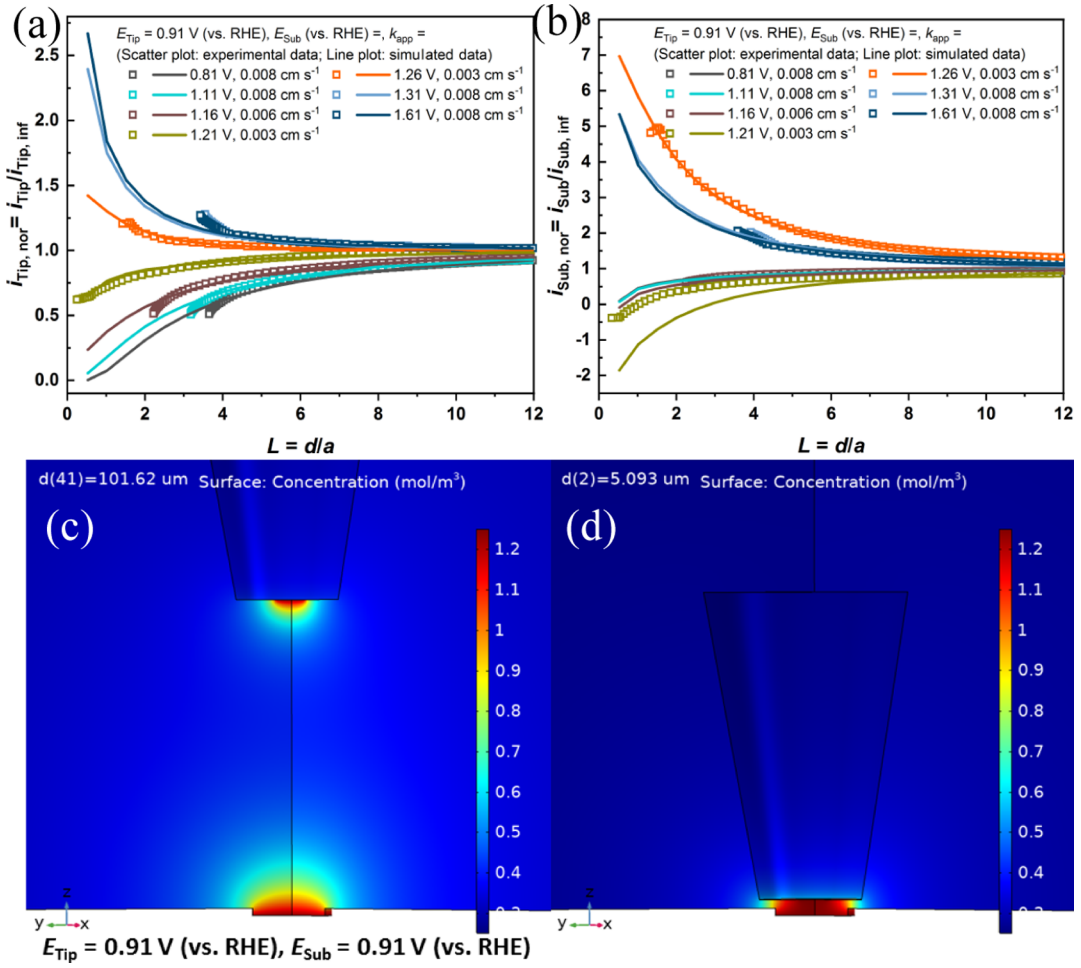

Figure 5. (a) Pt tip and (b) ITO UME substrate approach curves obtained at E_{Tip} = 0.91 V (vs RHE) and various E_{sub} and fitted with simulated data. Simulated 3D concentration profile of $IrCl_6^{3-}$ when the Pt tip is (c) far away from and (d) in the vicinity of the ITO UME surface at E_{Tip} = 0.91 V (vs RHE) and E_{Sub} = 0.91 V (vs RHE).

study at an individual UME without interferences from the others.

Based on our transparent ITO/FTO UME, a model semiconductor UME, TiO_2-FTO UME was developed by incorporating a facile hydrothermal process, where the formation mechanism of TiO_2 crystals has been previously reported to be a condensation reaction of Ti^{4+} hydrated octahedral monomers.[61] The surface morphology of TiO_2 on FTO at a macroscopic sample was characterized by SEM and is shown in Figure 2d. TiO_2 nanorods are uniformly formed on FTO with an estimated diameter of ∼100 nm. By comparing the optical microscopy images of bare FTO UMEs (Figure 2e) and TiO_2−FTO UMEs (Figure 2f), TiO_2 can be observed to uniformly and selectively grow on the FTO surface. Digital photos of the real FTO and TiO_2−FTO UMEs samples can be found in Figure S4.

Quantification of Interfacial Electron-Transfer Kinetics at ITO UME with SECM. Figure 3a,b illustrate the SECM-optical microscopy system for quantifying the PEC activities of micrometer-sized TiO_2 nanorods through a transparent UME. This system features flexible light illumination of a selected transparent UME in an inverted configuration while simultaneously collecting tip and substrate current signals and optical microscopy images. The EMCCD camera and 3-axis SECM tip positioning capabilities allow a rapid positioning of a Pt UME tip above the selected transparent UME.

The as-prepared ITO UME was employed as the substrate electrode in SECM and characterized for interfacial electron-transfer kinetics. The quantification study at our ITO UME platform was simplified by using an outer-sphere redox couple, $IrCl_6^{2-}/IrCl_6^{3-}$, which allows a fast and reversible one-electron transfer reaction. At a large tip-to-substrate distance (d), cyclic voltammetry (CV) curves of the Pt tip and ITO UME substrate in the bulk solution of 0.1 M Na_2SO_4 containing 1 mM K_2IrCl_6 at a scan rate of 10 mV s^{-1} are shown in Figure 4a. The ITO UME can achieve a similar steady-state reduction reaction of $IrCl_6^{2-}$ as Pt tip UME showing a diffusion-controlled liming current, i_{lim}, which indicates an efficient mass transport at its surface. A low anodic current appears at both the Pt tip and the ITO UME substrate owing to the spontaneous reduction of $IrCl_6^{2-}$ in the weakly acidic solution. This auto-reduction reaction accompanied by water oxidation has been previously reported.[62,63] The voltammetric behaviors are fitted with simulations to obtain the heterogeneous rate constants (k^0) of the redox reaction occurring at the Pt tip and the ITO UME, k_{Tip}^0 = 0.08 cm s^{-1} and k_{Sub}^0 = 0.008 cm s^{-1}, respectively.

Major parameters used for simulations such as formal potential ($E^{0'}$) and cathodic charge transfer coefficients (α) are

https://doi.org/10.1021/acs.analchem.1c02598
Anal. Chem. 2021, 93, 15886−15896

listed in Table S1. A smaller α_{Sub} of 0.3 compared to α_{Tip} of 0.5 indicates a less favorable asymmetric reduction behavior of $IrCl_6^{2-}$ at the ITO UME. According to the criterion of reversibility factor (Λ) proposed by Matsuda and Ayabe,[64] the calculated values of Λ are 50.1 (reversible) at the Pt tip and 5.01 (quasi-reversible) at ITO UME. Simulations were also employed to explore the effects of photoresist thickness (t_{pr}) and k_{Sub}^0 on the voltammetric behavior of ITO UME in the bulk solution (see Figures S6 and S7).

ITO UME obtained with microfabrication was then studied with a Pt tip to obtain SECM reactivity images in the feedback mode. In principle, the tip first needs to be positioned in close vicinity of the ITO UME surface, and d can be estimated by performing an approach curve measurement in a feedback mode above the photoresist layer (see Figure S8). Constant-height SECM images of the tip current (i_{Tip}) and the substrate current (i_{Sub}) are shown in Figure 4b,c, respectively. These images were obtained at d = 15 μm under the SG-TC mode, where the substrate potential (E_{Sub}) was held at 0.91 V to undergo the steady-state reduction reaction of $IrCl_6^{2-}$ and the tip potential (E_{Tip}) was held at 1.51 V for the steady-state reversed oxidation reaction. When the Pt tip comes to the vicinity of ITO UME, an increased amount of $IrCl_6^{3-}$ generated at ITO UME is collected by the tip for regenerating $IrCl_6^{2-}$, resulting in a positive feedback with increased i_{Tip} and i_{Sub}. The obtained SECM images show circular regions of increased i_{Tip} and i_{Sub} with diameters of around 35 and 25 μm representing the electroactive sizes of ITO UME and the Pt tip, respectively. The lateral resolution can be further improved by decreasing d or employing a smaller tip radius a in the experiment. The size of ITO UME is supposed to be ~2.5 times as large as that of the Pt tip based on the physical characterizations, whereas it is 1.4 extracted from the SECM reactivity images. This is reasonable when considering that the lateral resolution in SECM strongly depends on the size of the SECM tip. Here, the ITO UME is probed by a smaller-sized tip UME, while the Pt tip is probed by a larger-sized ITO UME on the relative motion, leading to a relatively lower lateral resolution. The tip collection efficiency (T-CE) in the SG-TC mode is shown in Figure 4d, indicating a maximum T-CE of 29.3% at the center of ITO UME.

Interfacial electron-transfer kinetics of the $IrCl_6^{2-}/IrCl_6^{3-}$ redox reaction at the ITO UMEs can be investigated by measuring the approach curves at a Pt tip above an ITO UME. With the aid of SECM imaging of ITO UME as described in Figure 4b, the Pt tip was placed directly above the center of ITO UME, where the maximum T-CE can be achieved, for approach curve measurements. The approach curve is represented by the normalized current $i_{nor.} = i/i_{inf.\ (d = \infty)}$ as a function of the normalized tip-to-substrate distance ($L = d/a$, where a is the electrode radius). As shown in Figure 5a,b, the tip and substrate approach curves are plotted at E_{Tip} = 0.91 V for the steady-state reduction of $IrCl_6^{2-}$ and various E_{Sub} from 0.81 to 1.61 V, respectively. Approach curves measured at more E_{Sub} values in between can be found in Figure S9. When the ITO UME is biased at E_{Sub} = 0.81 to 1.21 V, a negative feedback is observed at the Pt tip owing to a competitive consumption of $IrCl_6^{2-}$ at the ITO UME, reducing the steady-state diffusion rate of bulk $IrCl_6^{2-}$ towards the tip surface as L decreases. Substrate approach curves also show the negative feedback because the reduction reaction at the Pt tip competes with the one at the ITO UME. As shown in the simulated 3D concentration profiles of $IrCl_6^{3-}$ at E_{Tip} = 0.91 V and E_{Sub} = 0.91 V (Figure 5c,d), the competitive reduction reactions at the tip and substrate are illustrated by the increased concentration gradient at d = 0.593 μm compared to the one at d = 101.63 μm. In contrast, a positive feedback is created when the ITO UME is biased at E_{Sub} = 1.26 to 1.61 V due to the oxidation reaction of tip-generated $IrCl_6^{3-}$ at the ITO UME, enhancing the steady-state diffusion rate of redox species at the Pt tip. Substrate approach curves in this case show the positive feedback as well. The simulated 3D concentration profiles of $IrCl_6^{3-}$ at E_{Tip} = 0.91 V and E_{Sub} = 1.51 V demonstrate the decreased surface concentration gradient under the positive feedback condition (see Figure S10). The substrate collection efficiency (S-CE) versus L curve in this tip generation substrate collection (TG-SC) mode can be obtained at E_{Tip} = 0.91 V and E_{Sub} = 1.51 V, as shown in Figure S11.

Experimentally measured approach curves are fitted with simulated data based on the 2D axisymmetric geometry shown in Figure S3, which enables the quantification of potential-dependent apparent heterogeneous rate constant (k_{app}) of the $IrCl_6^{2-}/IrCl_6^{3-}$ redox reaction at the ITO UME. The discrepancy of the experimental approach curve from the simulation at low L values is associated with tip−substrate misalignment and the nonideal tip geometry and insulation.[65] k_{app} was simulated to be 0.008 cm s^{-1} when the ITO UME was biased for the steady-state reduction or oxidation reaction, which is consistent with the obtained k^0 from the simulation of bulk voltammetric current. However, k_{app} = 0.006, 0.003, and 0.003 cm s^{-1} were determined when the ITO UME was biased in the kinetically controlled region at E_{Sub} = 1.16, 1.21, and 1.26 V (η = −0.044, 0.006, and 0.056 V), respectively. Under the circumstances, the formation of redox species instead of diffusion becomes the rate-limiting step, leading to a slower mass transfer at the ITO UME than at the steady state, so the obtained k_{app} by fitting tip approach curves deviates from k^0, suggesting a slower interfacial electron-transfer kinetics at the ITO UME. Therefore, if too small an overpotential region is considered, the approach curve fitting in SECM leads to a misrepresentation of k^0. Potential-dependent apparent forward rate constants ($k_{app,\ f}$) were further calculated, as shown in Table S2.

Using the k_{app} obtained from the simulation of tip approach curves, the substrate approach curves are well fitted at E_{Sub} within or near the steady-state region. Technically, the substrate approach curves aim to determine the k_{app} at the Pt tip, so they are supposed to be constant at E_{Tip} = 0.91 V in our experimental setup no matter how the k_{app} at ITO UME is varied. However, the experimental substrate approach curve at E_{Sub} = 1.21 V shows a less significant negative feedback than the simulated data because of a slow formation rate-determining mass transfer, which deviates from the assumption of steady-state mass transport at the probing electrode in our theoretical simulation. The integrity of Pt and ITO UME after the approach curve test is further presented in Figures S12 and S13, and more related discussions can be found in the Supporting Information.

Quantification of Interfacial Charge-Transfer Kinetics of PEC Water Oxidation at TiO_2−FTO UME with the $IrCl_6^{2-}$ Redox Mediator and Direct Detection of O_2 Using SECM. For applying our transparent UME platform in a real semiconductor-based PEC process, the PEC water oxidation at TiO_2−FTO UME was investigated by SECM as a model system. As shown in Figure 6a, the photocurrent of the

https://doi.org/10.1021/acs.analchem.1c02598
Anal. Chem. 2021, 93, 15886−15896

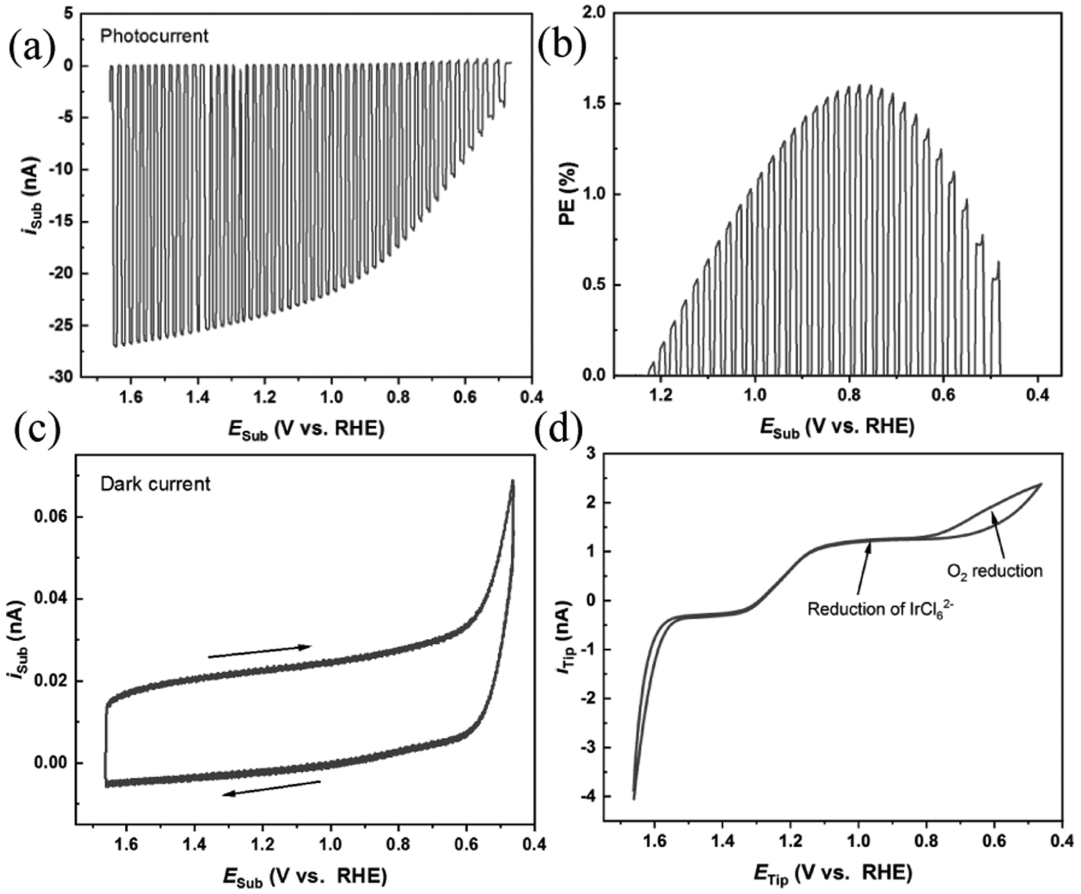

Figure 6. (a) Current vs potential curve and (b) PE estimation of TiO_2-FTO UME for PEC water oxidation in 0.1 M Na_2SO_4 containing 1 mM K_2IrCl_6 under chopped UV−vis light illumination (98.27 mW/cm^2). (c) CV curve of TiO_2−FTO UME in the dark. Scan rate: 50 mV s^{-1}. (d) Bulk CV curve of the Pt tip scanned at an extended potential range. Scan rate: 10 mV s^{-1}.

TiO_2−FTO UME increases with E_{Sub} in K_2IrCl_6-containing electrolyte due to the UV light sensitivity of TiO_2, which is an electron-rich semiconductor capable of producing photogenerated carriers upon light absorption. Negatively charged electrons in the conduction bands of TiO_2 can be favorably collected by the FTO substrate to form an anodic photocurrent when the holes are efficiently separated from the electrons to oxidize water for oxygen generation. The power efficiency (PE) of such photocurrent generation is dependent on the light absorptivity, charge transport, separation and collection efficiencies, and the surface reaction kinetics of water oxidation. PE at TiO_2−FTO UME can be estimated according to eq 1[66] and is plotted in Figure 6b.

$$\mathrm{PE}(\%) = \frac{J \times (1.23 - E_{\mathrm{Sub}})}{P_{\mathrm{Total}}} \times 100\% \quad (1)$$

where J (A/cm^2) is the photocurrent density extracted from Figure 6a and P_{Total} (W/cm^2) is the total light intensity focused on TiO_2−FTO UME. The estimated PE of TiO_2−FTO UME is at a maximum of 1.60%. Additionally, the light transmission of TiO_2−FTO in the UV light region (<400 nm) was estimated to be 16.7% by measuring the light intensity with the aid of a GG400 longpass filter. The CV curve of TiO_2−FTO UME measured in the dark does not show any visible redox reaction of $IrCl_6^{2-}/IrCl_6^{3-}$ (Figure 6c), which suggests that the TiO_2 coating layer is sufficiently thick to block direct redox activities of $IrCl_6^{2-}$ without light excitation. $IrCl_6^{2-}$ was selected for investigating PEC water oxidation due to its chemical stability in our electrolyte environment and has a distinct redox potential from O_2 produced from the photoelectrode surface.[54] The steady-state reduction of $IrCl_6^{2-}$ can avoid the potential range for O_2 collection unlike that of $Fe(CN)_6^{3-}$.[31] The CV curve of $IrCl_6^{2-}$ at the Pt tip within an extended potential range shows the reduction of solution-dissolved O_2 starting at below 0.85 V (Figure 6d), which allows the exclusive detection of steady-state $IrCl_6^{2-}$ reduction at an applied E_{Tip} of above 0.85 V showing no interference from O_2 reduction.

SECM reactivity imaging of TiO_2−FTO UME was performed at a constant-height feedback mode (Figure 7a). Here, the Pt tip was positioned at d = 22 μm and biased at 0.86 V for the steady-state reduction of $IrCl_6^{2-}$, and TiO_2−FTO UME was illuminated and biased at 0.86 V for PEC water oxidation. An increase of the measured i_{Tip} can be observed when the Pt tip is positioned near the TiO_2−FTO UME, indicating a positive feedback between the tip and substrate. It strongly suggests that the photogenerated charge carriers can oxidize not only water oxidation but also tip-generated $IrCl_6^{3-}$. No pronounced positive feedback is observed from the mapping of i_{Sub} owing to the overwhelming water oxidation photocurrent.

To quantify the interfacial charge-transfer kinetics of PEC water oxidation, we aligned the tip above the center of TiO_2−FTO UME and measured the tip and substrate approach curves under various E_{Sub} conditions (Figure 7b,c). The E_{Tip} was held at 0.86 V for steady-state reduction of $IrCl_6^{2-}$, while

https://doi.org/10.1021/acs.analchem.1c02598
Anal. Chem. 2021, 93, 15886−15896

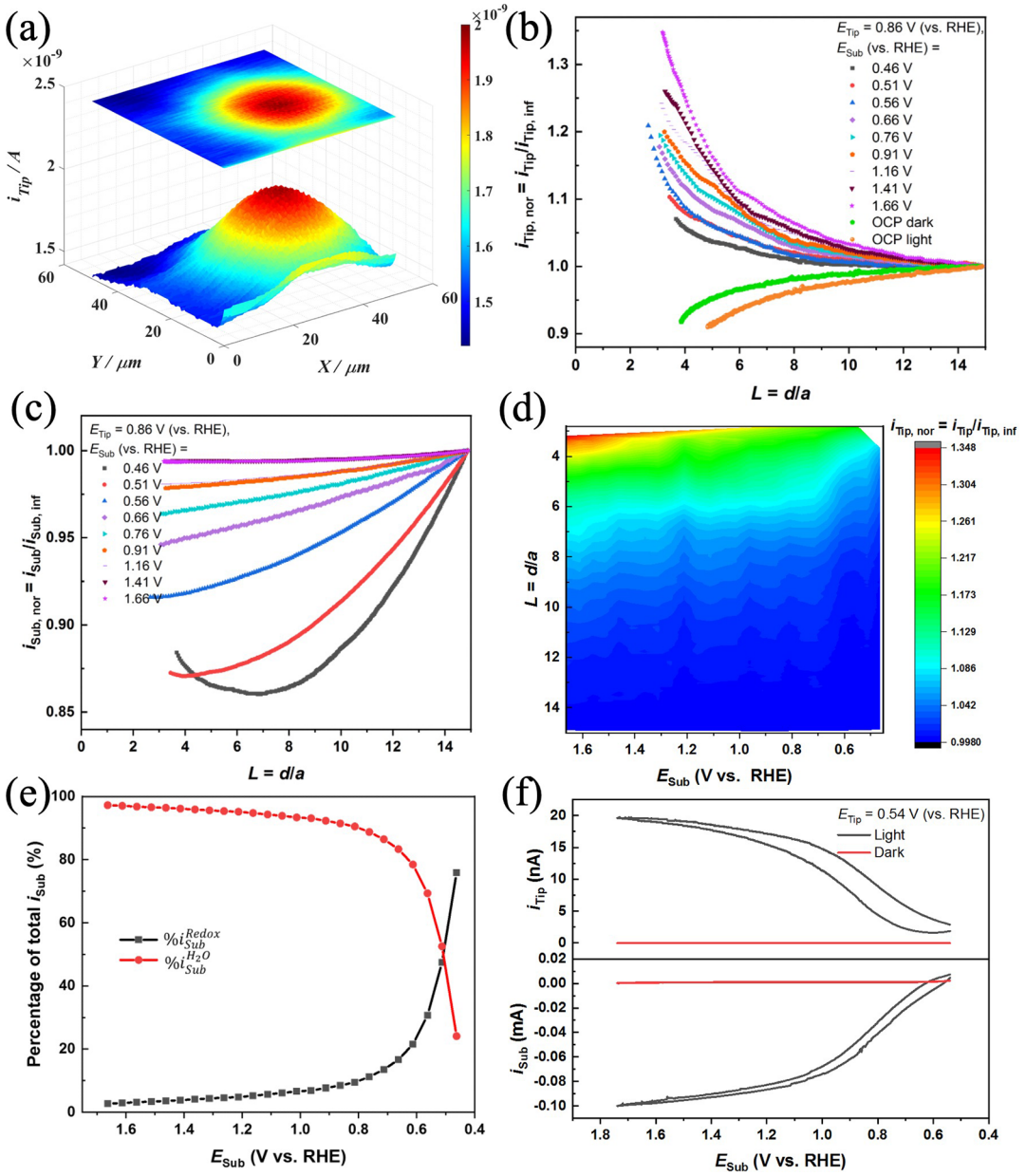

Figure 7. (a) SECM reactivity image (50 × 50 μm) of i_{Tip} under the constant-height feedback mode at d = 22 μm over the TiO_2−FTO UME. E_{Sub} = 0.86 V (vs RHE), and E_{Tip} = 0.86 V (vs RHE). Scan rate: 25 μm s^{-1}. The top image represents the projection onto the xy-plane. (b) Pt tip and (c) TiO_2−FTO UME substrate approach curves obtained with E_{Tip} = 0.86 V (vs RHE) and various E_{Sub} from OCP, 0.46 to 1.66 V (vs RHE) for PEC water oxidation. (d) Mapping of normalized tip current along with the normalized tip-to-substrate distance and the E_{Sub} extracted from (b) and Figure S14a. (e) Percentages of photocurrent contributions to $IrCl_6^{3-}$ oxidation ($\%i_{Sub}^{Redox}$) and water oxidation ($\%i_{Sub}^{H_2O}$) under various E_{Sub} obtained at L = 3.5. (f) Collection of products of PEC water oxidation at a large TiO_2−FTO UME substrate in the redox-free 0.1 M Na_2SO_4 electrolyte by the Pt tip biased at 0.54 V (vs RHE). Scan rate: 10 mV s^{-1}.

the E_{Sub} was selected at the open-circuit potential (OCP) and in the region of PEC water oxidation. Approach curves measured at more E_{Sub} values between 0.61 and 1.61 V can be found in Figure S14. When the TiO_2−FTO UME is at OCP without light excitation, a negative feedback can be observed at the tip approach curve which suggests a good curve fit by assuming an insulating TiO_2 surface (Figure S15). When the TiO_2−FTO UME is illuminated at OCP, the tip approach curve shows a more significant negative feedback, which is strongly attributed to the interfacial transfer of photogenerated electrons. Without an external potential bias, electrons are majority charge carriers and free to migrate to the TiO_2/electrolyte interface for the reduction of $IrCl_6^{2-}$, which competes with the same reaction at the Pt tip. Thus, this stronger negative feedback is resulted from the diffusion hindrance by the substrate surface as well as the competitive consumption of $IrCl_6^{2-}$ at TiO_2. Fujishima's group has reported a similar observation of $Fe(CN)_6^{3-}$ reduction at an unbiased illuminated TiO_2 surface by using SECM.[28]

When the TiO_2−FTO UME is positively biased from 0.46 to 1.66 V for PEC water oxidation, the tip approach curves show a positive feedback, indicating a facilitated mass transport at the TiO_2/electrolyte interface. It can be inferred that the local $IrCl_6^{3-}$ species are oxidized by photogenerated holes, leading to a transient increase of $IrCl_6^{2-}$ concentration. The positive feedback occurs starting at an E_{Sub} of 1.26 V at the conductive

https://doi.org/10.1021/acs.analchem.1c02598
Anal. Chem. 2021, 93, 15886−15896

ITO, whereas it can be observed here at semiconductor TiO_2 at an E_{Sub} of as early as 0.46 V. This owes to the positive potential shift of energy band edge near the surface of the n-type semiconductor under an electric field in the space charge region (called band bending). The actual TiO_2 surface potential is thus more positive than the one we applied in the bulk. Moreover, the positive feedback becomes increasingly prominent as E_{Sub} is enhanced from 0.46 to 1.66 V, suggesting a facilitated apparent heterogeneous electron-transfer kinetics as well as an increased charge carrier separation kinetics near the TiO_2 surface. This can be better visualized by mapping the integrated tip current along with L and E_{Sub} (Figure 7d), where the positive feedback becomes considerable as $L \leq \sim 6$.

However, the positive feedback in the substrate approach curves can be only observed at small values of E_{Sub} (from 0.46 to 0.56 V), and it is significantly masked by the large water oxidation current as E_{Sub} further increases (Figure 7c). The substrate approach curves exhibit an overall decreasing tendency as they are recorded, which can be explained by the charge recombination at trap sites of the TiO_2 surface. This charge recombination phenomenon becomes less severe as E_{Sub} increases.

As has been noted that negligible oxygen is reduced at the tip under an E_{Tip} of above 0.85 V, the positive feedback at the Pt tip exclusively represents the detection of $IrCl_6^{3-}$ oxidation at TiO_2-FTO UME. Knowing that the TiO_2 photocurrent i_{Sub} is contributed from both $IrCl_6^{3-}$ oxidation and water oxidation, their relative contributions can be quantitatively determined by applying a known S-CE (or i_{Sub}/i_{Tip}, extracted from the tip and substrate approach curves at an ITO UME, see Figure S11). The percentages of photocurrent contributions associated with $IrCl_6^{3-}$ oxidation ($\%i_{Sub}^{Redox}$) and water oxidation ($\%i_{Sub}^{H_2O}$) at L = 3.5 can be estimated according to eqs 2 and 3 and are plotted in Figure 7e.

$$\%i_{Sub}^{Redox} = \frac{i_{Tip}(L = 3.5) \times (i_{Sub}/i_{Tip})(L = 3.5)}{i_{Sub}(L = 3.5)} \times 100\% \quad (2)$$

$$\%i_{Sub}^{H_2O} = 1 - \%i_{Sub}^{Redox} \quad (3)$$

where i_{Sub}/i_{Tip} = 0.96 at L = 3.5. It can be observed that the contribution of $IrCl_6^{3-}$ oxidation to the total i_{Sub} reaches ~76% at a lower E_{Sub} of 0.46 V and decreases exponentially to ~3% as E_{Sub} increases to 1.66 V. The contribution of water oxidation behaves inversely. The relationship of i_{Sub} for $IrCl_6^{3-}$ oxidation and water oxidation at an E_{Sub} is important to be considered in the SECM quantification of overall interfacial charge-transfer kinetics at TiO_2–FTO UME.

Simulations of the tip approach curves were not performed here due to the unknown surface potentials under band bending conditions. Applying anodic E_{Sub} further increases the band bending in TiO_2.[67] An improved model with the consideration of photogeneration rates of electrons and holes and charge recombination rate will be also needed to fully understand the PEC performance of TiO_2 UME using the SECM quantification method. The integrity of the Pt tip and the enhanced photoactivity of TiO_2–FTO UME after the approach curve test were presented and are discussed in Figures S16 and S17.

To confirm the generation of the PEC water oxidation product (mainly O_2) without the interference from the redox mediator, a supplementary SECM study was conducted at a large TiO_2–FTO substrate in the redox-free 0.1 M Na_2SO_4 electrolyte. A Pt tip was positioned at d = 9 μm above the substrate by performing an approach curve measurement in the K_2IrCl_6-containing electrolyte, which was then replaced with a redox-free electrolyte (see Figure S18 for the respective CV curves). O_2 generated at TiO_2 during PEC water oxidation can be simultaneously collected by the Pt tip biased at 0.54 V for O_2 reduction in a SG-TC SECM mode. As shown in Figure 7f, the i_{Tip} measured under illumination increases at an enhanced E_{Sub}, indicating the O_2 generation during PEC water oxidation at TiO_2. In contrast, no cathodic i_{Tip} can be observed without photoexcitation.

Based on the above SECM approach curve results, the potential-dependent PEC water oxidation reaction mechanism at TiO_2 nanorods can be well illustrated (Figure 8). When

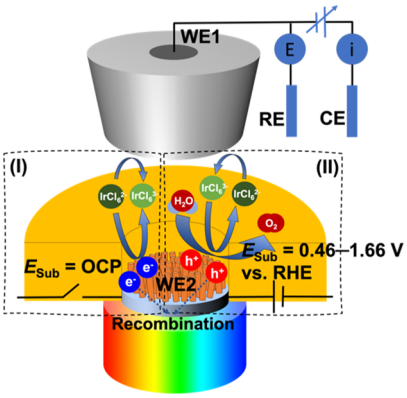

Figure 8. Schematic of the investigation of potential-dependent interfacial charge-transfer kinetics of PEC water oxidation at TiO_2 nanorods using the SECM technique. (I) Reduction of $IrCl_6^{2-}$ by photogenerated electrons under OCP; (II) simultaneous oxidation of water and $IrCl_6^{3-}$ by photogenerated holes when E_{Sub} = 0.46–1.66 V (vs RHE).

TiO_2 is in contact with the redox electrolyte with a different Fermi level, the interfacial charge transfer is required to equilibrate the interface. A low density of free charge carriers in TiO_2 results in a near-surface space charge region driven by an electric field.[68] In the absence of a substrate potential bias, the equilibrium electric field is not strong enough to efficiently separate the photogenerated electrons and holes. The charge recombination kinetics is faster than the charge separation kinetics, so the reduction of $IrCl_6^{2-}$ promoted by the majority of charge carriers (electrons) dominates at the TiO_2 surface. It thus creates a strong negative feedback at the Pt tip. When applying an external electric force toward the anodic direction, charge carriers are adequately separated by the electric field, allowing both water and $IrCl_6^{3-}$ oxidations by photogenerated holes at the TiO_2/electrolyte interface. As the external electric force becomes stronger (E_{Sub} increases from 0.46 to 0.71 V), charge separation and collection rates are further enhanced, yielding more efficient water oxidation and interfacial redox reaction. PEC current reaches a plateau with the minimum charge recombination under the external electric field of E_{Sub} = 0.71 V, which is determined by the incident light intensity and the intrinsic chracteristics of TiO_2 and its interface with he electrolyte. Further enhancement of water oxidation and redox reaction rates occurs at E_{Sub} = 1.21 V when the surface conductivity of TiO_2 is significantly increased. More charge

https://doi.org/10.1021/acs.analchem.1c02598
Anal. Chem. 2021, 93, 15886–15896

carriers in bulk TiO_2 are released under the very high electric field, leading to the added portion of water oxidation.

CONCLUSIONS

In summary, a transparent UME platform has been developed for SECM by a two-step photolithographic patterning incorporated with an ion milling treatment. The patterned UMEs are electrically isolated and individually have a 25 μm recessed disk-shaped geometry, allowing a quantitative study of interfacial electron-transfer kinetics of electrochemical redox reaction by measuring approach curves in the SECM technique and comparing with theoretical modeling in COMSOL Multiphysics. k_{Sub}^0 of 0.008 cm s^{-1} and α_{Sub} of 0.3 for the electrochemical reduction of $IrCl_6^{2-}$ at an ITO UME in 0.1 M Na_2SO_4 solution containing 1 mM K_2IrCl_6 have been confirmed by steady-state approach curve fitting. Collection efficiencies in both SG-TC and TG-SC modes are quantified by correlating tip and substrate reactivity images and approach curve measurements, respectively. FTO UME coated with TiO_2 nanorods is used as the model semiconductor UME for quantifying its interfacial photogenerated charge-transfer kinetics of PEC water oxidation in the feedback mode of SECM. The percentages of photocurrent contributions associated with redox reaction compared to water oxidation have been obtained to be ~76% at a low potential of 0.46 V and exponentially decrease to ~3% at a higher potential of 1.66 V. The transparent UME-SECM platform exhibits a great potential for studying interfacial charge-transfer kinetics of other electrochemical or PEC systems. This transparent UME-based SECM technique operating in other functional modes, particularly the surface interrogation mode,[46,52,54,69] will provide more insights into the reaction mechanism of a PEC system for advanced energy conversion and ultrasensitive chemical detection.

ASSOCIATED CONTENT

Supporting Information

The Supporting Information is available free of charge at https://pubs.acs.org/doi/10.1021/acs.analchem.1c02598.

SECM setup; principles of modeling and simulation; digital photos of UMEs; AFM measurement of photoresist thickness; Modeling geometry input and major parameters used for simulations; effect of photoresist thickness and heterogeneous rate constant on local mass transfer profiles and CVs; data fitting of tip approach curves at the insulating photoresist and unbiased TiO_2−FTO UME in the dark; supplementary tip and substrate approach curves at ITO UME and TiO_2−FTO UME; simulated 3D concentration profile of $IrCl_6^{3-}$ under positive feedback conditions; *L*-dependent S-CE in the TG-SC mode; calculations of potential-dependent apparent forward rate constants at ITO UME; integrity characterizations of ITO UME and TiO_2−FTO UME after the approach curve test; and Pt tip cyclic voltammograms measured with and without the redox mediator (PDF)

AUTHOR INFORMATION

Corresponding Author

Shanlin Pan − *Department of Chemistry and Biochemistry, The University of Alabama, Tuscaloosa, Alabama 35487, United States;* orcid.org/0000-0003-2226-9687; Phone: +1-205-348-6381; Email: span1@ua.edu; Fax: 1-205-348-9104

Author

Xiao Li − *Department of Chemistry and Biochemistry, The University of Alabama, Tuscaloosa, Alabama 35487, United States;* orcid.org/0000-0001-7647-717X

Complete contact information is available at: https://pubs.acs.org/10.1021/acs.analchem.1c02598

Author Contributions

The manuscript was written through the contributions of all authors. All authors have given approval to the final version of the manuscript.

Notes

The authors declare no competing financial interest.

ACKNOWLEDGMENTS

We acknowledge National Science Foundation (NSF) for supporting this work under Award Number CBET-2113505. We acknowledge the support from Dr. Alton Highsmith at the Micro Fabrication Facility of The University of Alabama for UME fabrication and Alabama Analytical Research Center (AARC) for SEM characterization. S.P. acknowledges the support of Marilyn Williams Elmore and John Durr Elmore Professor fellowship. We thank Dr. Jeetika Yadav for assisting in the SEM imaging of ITO UMEs. X.L. thanks the support of the "new" transportation research fund from Alabama Transportation Institute.

REFERENCES

(1) Shu, J.; Tang, D. *Anal. Chem.* **2019**, *92*, 363−377.
(2) Chen, D.; Zhang, H.; Li, X.; Li, J. *Anal. Chem.* **2010**, *82*, 2253−2261.
(3) Shu, J.; Qiu, Z.; Lv, S.; Zhang, K.; Tang, D. *Anal. Chem.* **2018**, *90*, 2425−2429.
(4) Wu, F.; Zhou, B.; Wang, J.; Zhong, M.; Das, A.; Watkinson, M.; Hing, K.; Zhang, D.-W.; Krause, S. *Anal. Chem.* **2019**, *91*, 5896−5903.
(5) Maeda, K.; Domen, K. *J. Phys. Chem. Lett.* **2010**, *1*, 2655−2661.
(6) Takanabe, K. *ACS Catal* **2017**, *7*, 8006−8022.
(7) Li, J.; Wu, N. *Catal. Sci. Technol.* **2015**, *5*, 1360−1384.
(8) Ni, M.; Leung, M. K. H.; Leung, D. Y. C.; Sumathy, K. *Renew. Sustain. Energy Rev.* **2007**, *11*, 401−425.
(9) Devadoss, A.; Sudhagar, P.; Terashima, C.; Nakata, K.; Fujishima, A. *J. Photochem. Photobiol., C* **2015**, *24*, 43−63.
(10) Kim, K.; Park, C. B. *Biosens. Bioelectron.* **2020**, *154*, 112075.
(11) Ryu, J.; Lee, S. H.; Nam, D. H.; Park, C. B. *Adv. Mater.* **2011**, *23*, 1883−1888.
(12) Xu, Y.; Wang, S.; Yang, J.; Han, B.; Nie, R.; Wang, J.; Wang, J.; Jing, H. *Nano Energy* **2018**, *51*, 442−450.
(13) Fujishima, A.; Honda, K. *Nature* **1972**, *238*, 37−38.
(14) Linsebigler, A. L.; Lu, G.; Yates, J. T., Jr. *Chem. Rev.* **1995**, *95*, 735−758.
(15) Bard, A. J.; Fan, F. R. F.; Kwak, J.; Lev, O. *Anal. Chem.* **1989**, *61*, 132−138.
(16) Kwak, J.; Bard, A. J. *Anal. Chem.* **1989**, *61*, 1221−1227.
(17) Sánchez-Sánchez, C. M.; Rodríguez-López, J.; Bard, A. J. *Anal. Chem.* **2008**, *80*, 3254−3260.
(18) Rodríguez-López, J.; Minguzzi, A.; Bard, A. J. *J. Phys. Chem. C* **2010**, *114*, 18645−18655.
(19) Jedraszko, J.; Michalak, M.; Jönsson-Niedziolka, M.; Nogala, W. *J. Electroanal. Chem.* **2018**, *815*, 231−237.
(20) Eckhard, K.; Chen, X.; Turcu, F.; Schuhmann, W. *Phys. Chem. Chem. Phys.* **2006**, *8*, 5359−5365.
(21) Sun, T.; Wang, D.; Mirkin, M. V. *Angew. Chem., Int. Ed.* **2018**, *57*, 7463−7467.

(22) Amatore, C.; Lefrou, C.; Pflüger, F. *J. Electroanal. Chem. Interfacial Electrochem.* **1989**, *270*, 43−59.
(23) Amatore, C.; Jutand, A.; Pflüger, F. *J. Electroanal. Chem. Interfacial Electrochem.* **1987**, *218*, 361−365.
(24) Glasscott, M. W.; Dick, J. E. *Anal. Chem.* **2018**, *90*, 7804−7808.
(25) Deng, Z.; Elattar, R.; Maroun, F.; Renault, C. *Anal. Chem.* **2018**, *90*, 12923−12929.
(26) Nishikawa, K.; Shinoda, K.; Kanamura, K. *J. Phys. Chem. C* **2020**, *124*, 22019−22024.
(27) Monteiro, M. C. O.; Jacobse, L.; Touzalin, T.; Koper, M. T. M. *Anal. Chem.* **2019**, *92*, 2237−2243.
(28) Maeda, H.; Ikeda, K.; Hashimoto, K.; Ajito, K.; Morita, M.; Fujishima, A. *J. Phys. Chem. B* **1999**, *103*, 3213−3217.
(29) Haram, S. K.; Bard, A. J. *J. Phys. Chem. B* **2001**, *105*, 8192−8195.
(30) Shen, Y.; Nonomura, K.; Schlettwein, D.; Zhao, C.; Wittstock, G. *Chem. Eur J.* **2006**, *12*, 5832−5839.
(31) Zhang, B.; Zhang, X.; Xiao, X.; Shen, Y. *ACS Appl. Mater. Interfaces* **2016**, *8*, 1606−1614.
(32) Yengantiwar, A.; Palanivel, S.; Archana, P. S.; Ma, Y.; Pan, S.; Gupta, A. *J. Phys. Chem. C* **2017**, *121*, 5914−5924.
(33) Neto, S. Y.; da Silva, F. G. S.; Souto, D. E. P.; Faria, A. R.; de Andrade, H. M.; de Cássia Silva Luz, R.; Kubota, L. T.; Damos, F. S. *Electrochem. Commun.* **2017**, *82*, 75−79.
(34) Ning, X.; Li, W.; Meng, Y.; Qin, D.; Chen, J.; Mao, X.; Xue, Z.; Shan, D.; Devaramani, S.; Lu, X. *Small* **2018**, *14*, 1703989.
(35) Wang, Q.; Wang, X.; Yu, Z.; Jiang, X.; Chen, J.; Tao, L.; Wang, M.; Shen, Y. *Nano Energy* **2019**, *60*, 827−835.
(36) Kumar, S.; Satpati, A. K. *Electrochim. Acta* **2021**, *368*, 137565.
(37) Xiong, H.; Guo, J.; Amemiya, S. *Anal. Chem.* **2007**, *79*, 2735−2744.
(38) Oleinick, A. I.; Battistel, D.; Daniele, S.; Svir, I.; Amatore, C. *Anal. Chem.* **2011**, *83*, 4887−4893.
(39) Lee, J.; Ye, H.; Pan, S.; Bard, A. J. *Anal. Chem.* **2008**, *80*, 7445−7450.
(40) Jang, J. S.; Lee, J.; Ye, H.; Fan, F.-R. F.; Bard, A. J. *J. Phys. Chem. C* **2009**, *113*, 6719−6724.
(41) Ye, H.; Lee, J.; Jang, J. S.; Bard, A. J. *J. Phys. Chem. C* **2010**, *114*, 13322−13328.
(42) Liu, G.; Liu, C.; Bard, A. J. *J. Phys. Chem. C* **2010**, *114*, 20997−21002.
(43) Hsu, H.-Y.; Ji, L.; Du, M.; Zhao, J.; Yu, E. T.; Bard, A. J. *Electrochim. Acta* **2016**, *220*, 205−210.
(44) Hsu, H.-Y.; Ji, L.; Du, M.; Zhao, J.; Yu, E. T.; Bard, A. J. *J. Phys. Chem. C* **2016**, *120*, 19890−19895.
(45) Shinde, P. S.; Peng, X.; Wang, J.; Ma, Y.; McNamara, L. E.; Hammer, N. I.; Gupta, A.; Pan, S. *ACS Appl. Energy Mater.* **2018**, *1*, 2283−2294.
(46) Ma, Y.; Shinde, P. S.; Li, X.; Pan, S. *ACS Omega* **2019**, *4*, 17257−17268.
(47) Conzuelo, F.; Sliozberg, K.; Gutkowski, R.; Grützke, S.; Nebel, M.; Schuhmann, W. *Anal. Chem.* **2017**, *89*, 1222−1228.
(48) Bae, J. H.; Nepomnyashchii, A. B.; Wang, X.; Potapenko, D. V.; Mirkin, M. V. *Anal. Chem.* **2019**, *91*, 12601−12605.
(49) Yu, Y.; Sundaresan, V.; Willets, K. A. *J. Phys. Chem. C* **2018**, *122*, 5040−5048.
(50) Yu, Y.; Wijesekara, K. D.; Xi, X.; Willets, K. A. *ACS Nano* **2019**, *13*, 3629−3637.
(51) Schorr, N. B.; Counihan, M. J.; Bhargava, R.; Rodríguez-López, J. *Anal. Chem.* **2020**, *92*, 3666−3673.
(52) Kim, J. Y.; Ahn, H. S.; Bard, A. J. *Anal. Chem.* **2018**, *90*, 3045−3049.
(53) Zigah, D.; Rodríguez-López, J.; Bard, A. J. *Phys. Chem. Chem. Phys.* **2012**, *14*, 12764−12772.
(54) Park, H. S.; Leonard, K. C.; Bard, A. J. *J. Phys. Chem. C* **2013**, *117*, 12093−12102.
(55) Acharya, S.; Lancaster, M.; Maldonado, S. *Anal. Chem.* **2018**, *90*, 12261−12269.
(56) Ma, Y.; Highsmith, A. L.; Hill, C. M.; Pan, S. *J. Phys. Chem. C* **2018**, *122*, 18603−18614.
(57) Ma, Y.; Highsmith, A. L.; Pan, S. *ECS Trans.* **2018**, *85*, 1155.
(58) Qi, W.; Du, J.; Peng, Y.; Wu, W.; Zhang, Z.; Li, X.; Li, K.; Zhang, K.; Gong, C.; Luo, M.; Peng, H. *Mater. Chem. Phys.* **2018**, *207*, 435−441.
(59) *COMSOL Multiphysics*: Burlington, MA, accessed Feb 1998, 9, 2018.
(60) Dickinson, E. J. F.; Ekström, H.; Fontes, E. *Electrochem. Commun.* **2014**, *40*, 71−74.
(61) Zhang, J.; Sun, P.; Jiang, P.; Guo, Z.; Liu, W.; Lu, Q.; Cao, W. *J. Mater. Chem. C* **2019**, *7*, 5764−5771.
(62) Peixoto Cabral, J. M. *J. Inorg. Nucl. Chem.* **1964**, *26*, 1657−1669.
(63) Weusten, S. J. C.; de Groot, M. T.; van der Schaaf, J. *J. Electroanal. Chem.* **2020**, *878*, 114512.
(64) Matsuda, H.; Ayabe, Y. *Ber. Bunsen-Ges. Phys. Chem.* **1955**, *59*, 494−503.
(65) Shen, M.; Arroyo-Currás, N.; Bard, A. J. *Anal. Chem.* **2011**, *83*, 9082−9085.
(66) Chen, Z.; Jaramillo, T. F.; Deutsch, T. G.; Kleiman-Shwarsctein, A.; Forman, A. J.; Gaillard, N.; Garland, R.; Takanabe, K.; Heske, C.; Sunkara, M.; McFarland, E. W.; Domen, K.; Miller, E. L.; Turner, J. A.; Dinh, H. N. *J. Mater. Res.* **2010**, *25*, 3−16.
(67) Paramasivam, I.; Jha, H.; Liu, N.; Schmuki, P. *Small* **2012**, *8*, 3073−3103.
(68) Zhang, Z.; Yates, J. T., Jr *Chem. Rev.* **2012**, *112*, 5520−5551.
(69) Simpson, B. H.; Rodríguez-López, J. *Electrochim. Acta* **2015**, *179*, 74−83.

https://doi.org/10.1021/acs.analchem.1c02598
Anal. Chem. 2021, 93, 15886−15896